Biophysical Journal Volume 81 January 2002 493–508

Three-Dimensional High-Resolution Second-Harmonic Generation Imaging of Endogenous Structural Proteins in Biological Tissues

Paul J. Campagnola,*‡ Andrew C. Millard,*‡ Mark Terasaki,*‡ Pamela E. Hoppe,§ Christian J. Malone,¶ and William A. Mohler†‡

*Department of Physiology and †Department of Genetics and Developmental Biology and ‡Center for Biomedical Imaging Technology, University of Connecticut Health Center, Farmington, Connecticut 06030; §Department of Genetics, Washington University School of Medicine, St. Louis, Missouri 63110; and ¶Laboratory of Molecular Biology, University of Wisconsin, Madison, Wisconsin 53706 USA

ABSTRACT We find that several key endogenous protein structures give rise to intense second-harmonic generation (SHG)—nonabsorptive frequency doubling of an excitation laser line. Second-harmonic imaging microscopy (SHIM) on a laser-scanning system proves, therefore, to be a powerful and unique tool for high-resolution, high-contrast, three-dimensional studies of live cell and tissue architecture. Unlike fluorescence, SHG suffers no inherent photobleaching or toxicity and does not require exogenous labels. Unlike polarization microscopy, SHIM provides intrinsic confocality and deep sectioning in complex tissues. In this study, we demonstrate the clarity of SHIM optical sectioning within unfixed, unstained thick specimens. SHIM and two-photon excited fluorescence (TPEF) were combined in a dual-mode nonlinear microscopy to elucidate the molecular sources of SHG in live cells and tissues. SHG arose not only from coiled-coil complexes within connective tissues and muscle thick filaments, but also from microtubule arrays within interphase and mitotic cells. Both polarization dependence and a local symmetry cancellation effect of SHG allowed the signal from species generating the second harmonic to be decoded, by ratiometric correlation with TPEF, to yield information on local structure below optical resolution. The physical origin of SHG within these tissues is addressed and is attributed to the laser interaction with dipolar protein structures that is enhanced by the intrinsic chirality of the protein helices.

INTRODUCTION

Second-harmonic generation (SHG) is beginning to emerge as a powerful contrast mechanism in nonlinear optical microscopy. SHG was first demonstrated by Kleinman in crystalline quartz in 1962 (Kleinman, 1962), and, since that time, has been commonly used to frequency double pulsed lasers to obtain shorter wavelengths. Shortly thereafter, SHG from interfaces was discovered by Bloembergen in 1968 (Bloembergen et al., 1968), and, since, has become a standard spectroscopic tool for characterizing surfaces and probing dynamics at interfaces (for reviews, see Shen, 1989; Eisenthal, 1996). In 1974, Hellwarth first integrated SHG into an optical microscope to visualize the microscopic crystal structure in polycrystalline ZnSe (Hellwarth and Christensen, 1974). This concept was also demonstrated by Sheppard in 1977 (Sheppard et al., 1977) and again more recently with modern imaging equipment and laser sources (Gauderon et al., 1998). In this paper, we describe the use of SHG to obtain high-resolution three-dimensional (3D) images of endogenous arrays of collagen, acto-myosin, and tubulin in a wide variety of species and cell and tissue types.

SHG is a second-order nonlinear optical process that has symmetry constraints confining signal to regions lacking a center of symmetry. Membranes lack such inversion symmetry, and these interfaces can therefore be imaged with great specificity by SHG. In prior work, we showed the utility of second-harmonic generation imaging microscopy (SHIM) in imaging the plasma membranes of several tissue-culture cell lines (Ben-Oren et al., 1996; Peleg et al., 1999; Campagnola et al., 1999). We pointed out that, because SHG is a nonlinear optical process, this form of excitation retains the benefits of two-photon excitation fluorescence (TPEF) microscopy: due to the peak power requirements for these processes, sufficient power density in a microscope only occurs at the focal point. This results in intrinsic 3D sectioning without the use of a confocal aperture (Denk et al., 1990), and, as a consequence, out-of-plane photobleaching and photo-toxicity are greatly reduced. In this prior work, the cells were stained with a lipophilic dye to generate sufficient contrast. Although out-of-plane photobleaching and photo-toxic effects are reduced in nonlinear optical excitation schemes, in-plane damage still results, largely from formation of singlet oxygen free radicals upon photobleaching of fluorescent dyes. Thus, it would be desirable to obtain 3D, high-resolution (near diffraction limited) images at high contrast without relying upon fluorescence.

In a series of rigorous experiments, Freund et al. (1986) used SHG microscopy in 1986 to study the endogenous collagen structure in a rat tail tendon at ~50-μm resolution. More recently, in a reflection mode setup, Alfano and coworkers used stage-scanning laser excitation to image SHG within muscle and connective tissue, where frame rates of several hours were required (Guo et al., 1997, 1999). Here, we present work that uses a laser-scanning transmission-mode microscope and extends this imaging

---

Received for publication 1 May 2001 and in final form 26 September 2001.

Address reprint requests to Paul J. Campagnola, University of Connecticut Health Center, Center for Biomedical Imaging Technology MC-1507, Farmington, CT 06030. Tel.: 860-679-4354; Fax: 860-679-1039; E-mail: campagno@neuron.uchc.edu.

0006-3495/02/01/493/16 $2.00

concept to higher resolution (~1 μm) and much higher rates of image acquisition (1 frame per second). We show that bright, high-resolution 3D SHG images of structural proteins within connective tissue, muscle, and mitotic spindles can be obtained at confocal-like frame rates.

Several aspects make this form of microscopy very powerful. Because the excitation uses near-infrared wavelengths, this method is well suited for studying intact tissue samples because excellent depths of penetration can be obtained. For example, we have acquired optical sections throughout 550 μm of mouse muscle tissue. Information about the organization of protein matrices at the molecular level can be extracted from SHG imaging data in several ways. Because the SHG signals have well-defined polarizations, SHG polarization anisotropy can be used to determine the absolute orientation and degree of organization of proteins in tissues. In addition, two-photon-excited fluorescence images can be collected in a separate data channel simultaneously with SHG. Correlation between the SHG and TPEF images provides the basis not only for molecular identification of the SHG source but also for probing the radial and lateral symmetry within structures of interest. Based on the physical nature of SHG contrast, we suggest that the SHG signals arise from dipolar interactions that are enhanced by the intrinsic chirality in higher-order protein helices, making SHIM quite distinct from other optical-imaging techniques.

MATERIALS AND METHODS

Microscopy equipment and physical measurements

A detailed description of the SHG/TPEF microscope has been given previously (Campagnola et al., 1999) and only a brief outline will be provided here. The SHG imaging experiments were performed on modified Biorad MRC600 confocal scan head mounted on a Zeiss upright microscope. The laser system is a Coherent argon ion (Innova 310, Coherent, Santa Clara, CA) pumped femtosecond titanium sapphire oscillator (900-F, Coherent), characterized by pulse width of approximately100 fs at 76 MHz repetition rate at 850 nm. Average powers at the sample were between 1 and 50 mW. Because SHG is a coherent process, the signal wave copropagates with the laser and is collected in a transmitted light configuration. A long working distance 40 × 0.8 N.A. water immersion lens (Zeiss, Zeiss, Jena, Germany) and a 0.9 N.A. condenser (Zeiss) are used for excitation and signal collection, respectively. The 1 mrad divergence of the ti:sapphire laser was compensated before the scan head. There is essentially no dispersion at 850 nm and thus no external precompensation was used to compensate for the minimal group delay in the scan head or objective. When applicable, the TPEF signal is descanned and collected with the pinhole aperture fully opened and detected simultaneously with the SHG. The SHG signal is first reflected with a 425-nm hard reflector (bandwidth ± 25 nm), then isolated from the laser fundamental and any fluorescence by 1 or 2 mm color glass (BG-39, CVI, Albuquerque, NM) and a short-wave pass filters (450 nm), respectively, and detected by a photon counting photomultiplier module (Hamamatsu 7421, Hammamatsu, Bridgewater, NJ). The TTL pulses from this module are integrated by the Biorad acquisition electronics. Data acquisition times were between 1 and 4 s per 768 × 512 frame, and images were acquired either as single frame, or as a result of 3 Kalman averages. The microscope is equipped with a fiber-based spectrometer to also collect spectra (Ocean Optics, USB2000, Ocean Optics, Dunelin, FL). Spectra are collected in the following way: A low-zoom SHG image is acquired, and then zoomed in 100-fold, corresponding to an area of 6 μm^2. The signal is then directed onto the fiber and the spectrum is acquired, with integration times of 25 ms to 2.5 s, depending on the sample.

SHG polarization anisotropy measurements were made with a Glan Laser Polarizer (GLP, CVI), where the data were obtained by maintaining the same input laser polarization and obtaining images with the GLP oriented both parallel and perpendicular to the laser fundamental. The intensities of the resulting images were integrated using Imagequant (Molecular Dynamics, Sunnyvale, CA).

Specimens and sample preparation

Scales plucked from live black tetra fish (*Gymnocorymbus ternetzi)* were provided by Vladimir Rodionov (University of Connecticut Health Center).

Mouse tissues were dissected from freshly sacrificed animals (provided by Ivo Kalajzic, University of Connecticut Health Center), mounted in 3% agarose on a glass slide under a 1.5-thickness coverslip, and imaged within 1 h of sample preparation. *Caenorhabditis elegans* worms were mounted live on a glass slide upon a pad of 3% agarose, and were sealed under a 1.5-thickness coverslip using a fillet of melting-point temperature bath oil (Sigma, St. Louis, MO). N2 (Bristol) was used as a wild type strain.

C. elegans strain RW1596 expressing GFP::MHC A was constructed as follows. A green fluorescent protein (GFP) tag was inserted at the initiator methionine in a cloned copy of the *myo-3* gene, resulting in deletion of two amino acids from myosin heavy chain A (MHC A). The coding sequence for GFP was amplified from PD95.69 (A. Fire, S. Xu, J. Ahnn, G. Seydoux, personal communication) using primers (written 5′ to 3′) L2617 *TAGATCCATCTAGA*AATGAGTAAAGGAGAAG and M3381 *TTCGAATGCGTCTGGATT*TTTGTATAGTTCATCCAT, where italicized bases represent *myo-3* sequence. The PCR product was digested with *Xba*I and BsmI, and cloned into digested pPH23aP1. The full-length MHC A construct was generated using sequences from pJK26a as described (Hoppe and Waterston, 1996). Transgenic lines were generated by injecting wild-type N2 worms with a 200 ng/μl DNA solution containing 1% myosin construct DNA from two independent clones, and 99% the *rol-6* co-injection marker pRF4 (Mello et al., 1991). The extra-chromosomal array *stEx30* was crossed into the null mutant *myo-3(st386)* to make strain RW1596. The array has sufficient rescuing activity to maintain the null mutant line and displays normal GFP::MHC A localization in the adult, although expression of the transgene causes some frequency of embryonic lethality (P. E. Hoppe and R. H. Waterston, unpublished observations). Strain FC34 was created by crossing the array *stEx30* from RW1596 into the MHC B null mutant *unc-54(e190)*. The preparation of *C. elegans* strain WH204 expressing β-tubulin::GFP was previously described (Strome et al., 2001).

Image processing

Images and image stacks acquired in BioRad .PIC format were imported into NIH Image v1.62 (developed by Wayne Rasband and the National Institutes of Health and available at http://rsb.info.nih.gov/NIH-image/). Contrast enhancement, maximum-point projections, and reslicing were performed using existing functions of NIH Image. Dual-channel overlays and final figures were created and edited within Adobe Photoshop v5.0.

FIGURE 1 SHG optical section from an isolated scale of black tetra fish, *G. ternetzi*. This specimen was used for most quantitative and spectroscopic studies of optical response. Laser power was attenuated substantially to avoid saturation of the detector. Scale bar = 50 μm.

RESULTS

Biological observations of SHG within tissues and cells

Connective tissue

Prior imaging and spectroscopic work by Freund et al. (1986) and Kim et al. (1999, 2000), respectively, showed that collagen possesses a large second-order nonlinear susceptibility. This observation suggested the possibility of using SHG to image connective tissue at high resolution. Figure 1 shows a single-frame SHG image of a fish scale where the size scale is 330 × 220 μm and acquisition time was 1 s. The fish scale is composed in large part of dense collagen fibrils, and is expected to yield a bright signal. Indeed the laser was attenuated to ~1 mW average power to avoid saturation of the integration electronics. By contrast, essentially no autofluorescence was observed at the incident intensity (data not shown). These SHG signals from connective tissues are the brightest that we have observed from any sample, far exceeding those obtained from stained lipid membranes, and, in fact, are sufficiently bright to see by eye if projected onto a white card.

The SHG and simultaneously acquired two-photon excited autofluorescence from an intact region of a mouse ear containing hair follicles are shown in Fig. 2, *A* and *B*, respectively. A two-color overlay of the two channels is shown in Fig. 2 *C*, where the SHG and TPEF channels are violet and green, respectively. The SHG (*A*) arises from the dermal collagen matrix, whereas the TPE autofluorescence (*B*) is detected both in the hair shaft and in cells of the epidermis (regular polygons). These images provide totally separate but complimentary information. Although keratin is well known to be strongly autofluorescent, collagen produces essentially no TPEF signal. By contrast, collagen is an efficient SHG source, whereas the keratin in the hair shafts and epidermis are invisible by SHG. Figure 2 *D* is an *xz* section through a hair follicle, further demonstrating the spatial separation of the SHG and TPEF from these two protein species.

Muscle tissue

The low-resolution observations of Guo et al. (1997) indicated that a significant source of SHG lies within striated muscle. We examined mouse skeletal muscle to ask more precisely which structures were responsible for SHG emission. A remarkable attribute of SHG imaging in muscle tissue was the intrinsic deep optical sectioning. Because SHG is a nonlinear form of excitation, signal arises only from the point of focus. Furthermore, excitation in the near infrared suffers less scattering than visible light and results in improved resolution deep within dense tissue. We found that detailed, high-contrast features could be resolved in SHIM optical sections throughout the full ~550-μm thickness of a freshly dissected, unfixed sample of mouse lower leg muscle (Fig. 3 *A*). Figure 3 *B* shows an optical section at a depth 14 μm into the sample, revealing intense SHG from a matrix of collagen fibrils (*black arrow*) in the epimysium layer surrounding muscle fibers. In the same image, contractile muscle cells grazed by this optical section produced bright SHG in a pattern clearly related to the period of sarcomeric repeats in the myofilament lattice (*white arrowhead*). A second optical section at a depth of 24 μm (Fig. 3 *C*) shows the sarcomere band pattern of SHG extending continuously across the full width of muscle fibers. Other fine details of the internal tissue structure are also visible. A breach in the band pattern (*white arrow*) indicates a tear in the myofilament lattice. A thin layer of extracellular matrix (perimysium) separating fiber groups within the muscle appears in cross-section (*white arrowhead*). A third optical section at a depth of 250 μm (Fig. 3 *D*) showed the orientation and packing of a more proximal (*right side of image*) and a more distal (*left side*) muscle body, separated by a thick layer of matrix (*white arrow*). Although SHG from individual collagen bundles was substantially brighter than myofilament SHG, signals were similar enough for resolution of both types of structures in the same image scan. Furthermore, because collagen-based features were much rarer than the ubiquitous sarcomeric structure, the majority of the SHG produced by muscle tissue arises from the myofilament lattice.

To characterize the physical nature and molecular source of muscle-derived SHG more specifically, we then imaged muscle within the optically compliant and genetically tractable model organism *C. elegans*. Polarization microscopy has often been used to observe the birefringence of ordered structural proteins, including those of contractile muscle (Inoue, 1986; Waterston, 1988). To examine the relationship of birefringence to SHG, we compared images of *C. elegans* muscle produced by a polarization microscope to optical sections produced by SHIM (Fig. 4, *A* and *B*, respectively). Although somewhat comparable, the polarization and SHG microscopes do not produce exactly the same patterns of contrast. Both modes reveal bright bands with dim central stripes. Yet the SHG bright bands appear relatively broader than the anisotropic A bands seen by polarization microscopy. The dark region between bright SHG bands (*arrow*) is devoid of bright nodular signals corresponding to dense bodies in the isotropic band of the polarization image. Thus, there is no simple one-to-one correspondence between SHG and polarization images, although the same structures (in this case, thick filaments) often generate both effects. This may be because the contrast in a polarization scope image arises from linear birefringence and is only seen between orthogonal polarizers. By contrast, SHG signals can be seen with various combinations of input and output polarizations, and indeed, these data can be used to extract the molecular orientation (Shen, 1989). Furthermore, SHG is a second-order phenomenon and thus depends on the square of the molecular concentration, rather than the linear process observed in a polarization microscope.

The benefits of SHIM optical sectioning are apparent even in relatively thin (~100 μm) *C. elegans*. The SHG image in Fig. 4 *B* was acquired in a region overlying and immediately adjacent to the pharyngeal muscle, visible in grazing section as a dim radial array at the bottom. Acquisition of similar detail in this region by conventional polarization microscopy would be difficult or impossible because of intense out-of-focus glare from the underlying pharynx.

To explore the molecular source of SHG within the myofilament lattice, we combined SHG/TPEF to observe muscle in a *C. elegans* strain expressing GFP::MHC A, the minor MHC isoform known to be restricted to the longitudinal mid-zone of thick filaments (Waterston, 1988; Miller et al., 1983). Figure 5, *A* and *B*, show simultaneously

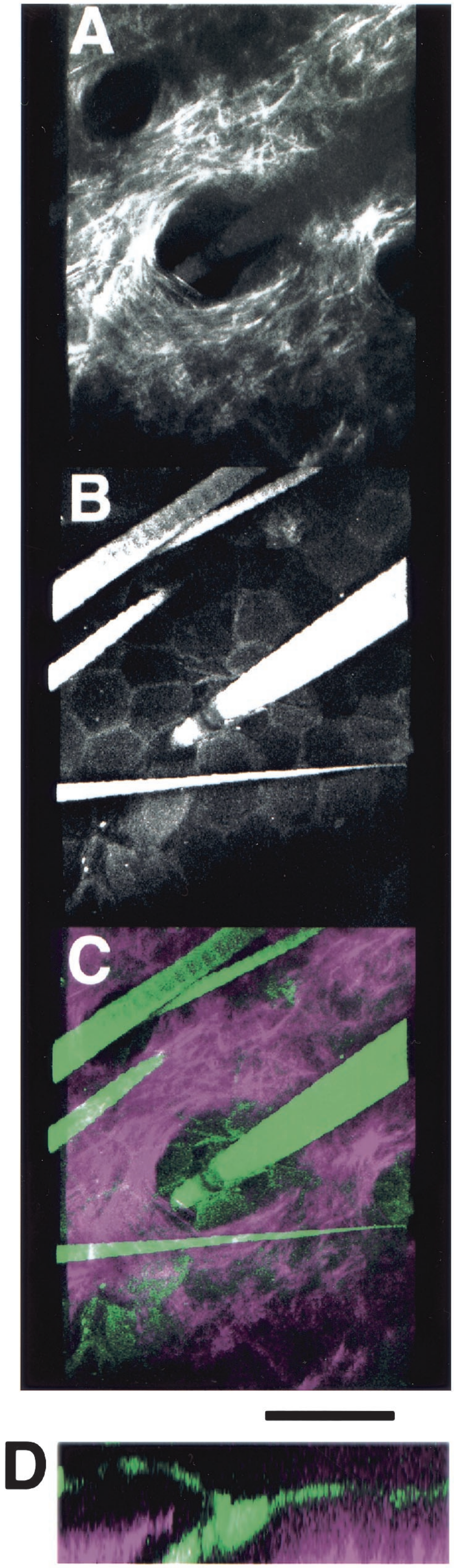

FIGURE 2 Dual-mode 3D imaging of endogenous SHG and fluorescence in tissue layers of a mouse ear. A full-thickness, freshly dissected sample of mouse ear was imaged simultaneously by SHG and TPEF. Stacks of optical sections were recorded for each channel. (*A*) SHG signal from deep, collagen-rich layer within dermis. Note the complete absence of signal from the central hair follicle, in contrast with the dense arrangement of fibrils in the bulk of the deep tissue. Extremely high absorbance by the overreaching hairshafts (see *B*) creates a shadowing of SHG signal in the upper right and left corners of the frame. (*B*) TPEF autofluorescence signal from keratin-rich hair shafts and epidermis. Note the continuous layer of epidermal cells closely surrounding the central hair shaft. (*C*) Color overlay of both SHG (*violet*) and TPEF (*green*) channels, allowing spatial correlation of the complementary signals. (*D*) *xz* section through hair follicle in center of panel *C*. In both *C* and *D*, it is apparent that the keratin-rich epidermal layer completely encloses the region above the collagen-negative hair follicle. Scale bar = 50 μm.

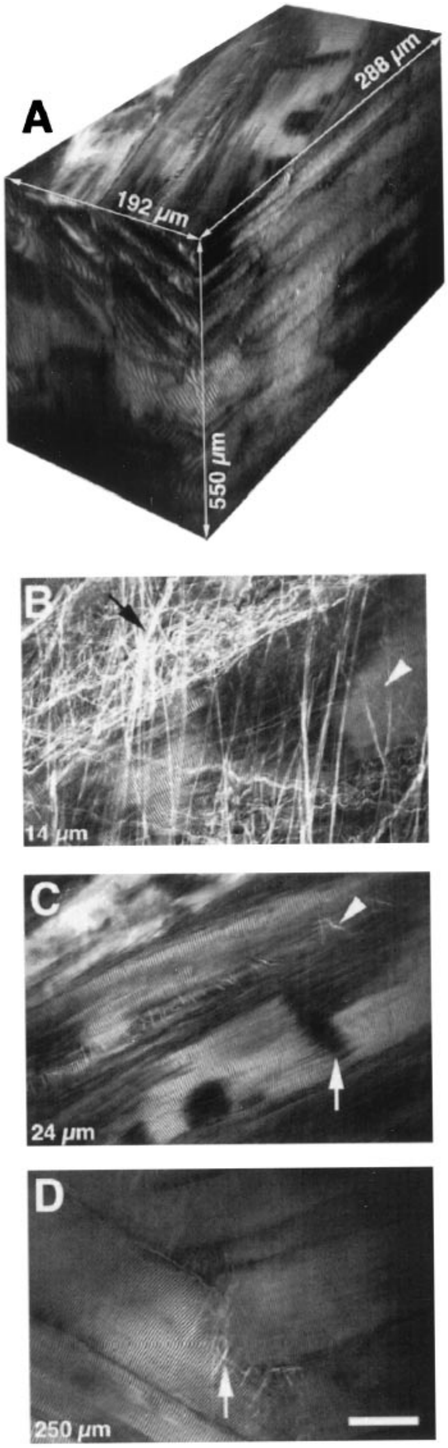

FIGURE 3 SHG imaging of extracellular and intracellular structures within native muscle tissue. A dissected sample of mouse lower leg muscle was optically sectioned through its full thickness of ~550 μm. (*A*). Graphic representation of the imaged volume of tissue. *xy* (*top*), *yz* (*left*), and *xz* (*right*) sections from the boundaries of the volume are shown. Dimensions are indicated, and are not portrayed proportionally; note that the *z* axis is particularly compressed in this model. (*B*) Extracellular matrix (epimysium) surrounding muscle fibers. An optical section at a depth 14 μm into the sample shows a web of presumptive collagen fibrils (*black arrow*) in the layer above muscle fibers. Note the muscle sarcomere pattern (*white arrowhead*) obtained by grazing of this optical section just beneath the surface of some fibers. Relative signal intensities from collagen and actomyosin can be compared in (*B*, *C*, *D*). (*C*) Myofilament lattice structure and interfiber matrix arrangement within muscle tissue. An optical section at a depth of 24 μm into the sample shows continuous repetitive sarcomeric pattern of SHG across the full width of muscle fibers. A breach in continuity of the pattern (*white arrow*) most likely resulted from tensile stress imposed during sample preparation. A thin layer of extracellular matrix (perimysium) separating fiber groups within the muscle is seen in cross-section (*white arrowhead*). (*D*). Deep section within muscle tissue. An optical section at a depth of 250 μm into the sample again shows the sarcomeric pattern and extracellular matrix. A transition between two distinct muscles is apparent in the different orientations of more proximal (*right side* of image) and more distal (*left side*) obliquely sectioned fibers separated by a thick layer of matrix (*white arrow*). Scale bar = 50 μm in (*B*, *C*, *D*).

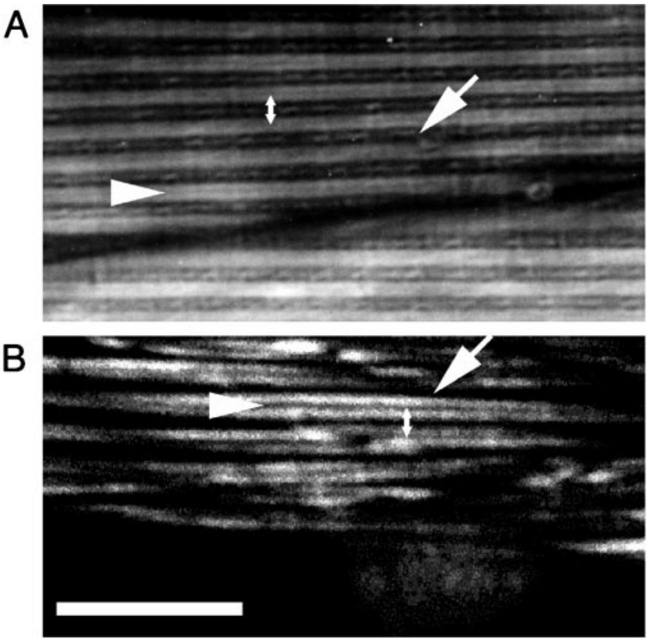

FIGURE 4 Comparison of polarization and SHG microscopy in nematode muscle. Body wall muscle of live *C. elegans* was imaged by both methods and is shown at identical magnification in (*A*) and (*B*). Double arrows indicate spacing between centers of adjacent sarcomere A bands in both panels. (*A*) Polarization image. Bright A bands are characterized by a dim central stripe (*arrowhead*). The dark I-band region is punctuated by birefringent dense bodies (*arrow*). (*B*). SHG image. Bright bands show a pronounced dark central stripe (*arrowhead*). The bright bands appear relatively broader than A bands seen by polarization microscopy. The dark region between bright bands (*arrow*) is devoid of nodular signal corresponding to dense bodies. Note that the SHG image was acquired in a region immediately adjacent to the pharygeal muscle, visible in grazing section as a dim radial array in the bottom of (*B*). Acquisition of similar detail in this region by polarization microscopy would be impossible because of intense out-of-focus glare from the underlying pharynx. Scale bar = 10 μm.

acquired SHIM and TPEF images, respectively. High magnification reveals that the signals are spatially distinct and complementary, as seen in the two color overlay in Fig. 5 *C*. Fluorescence from GFP::MHC A is observed in the dim

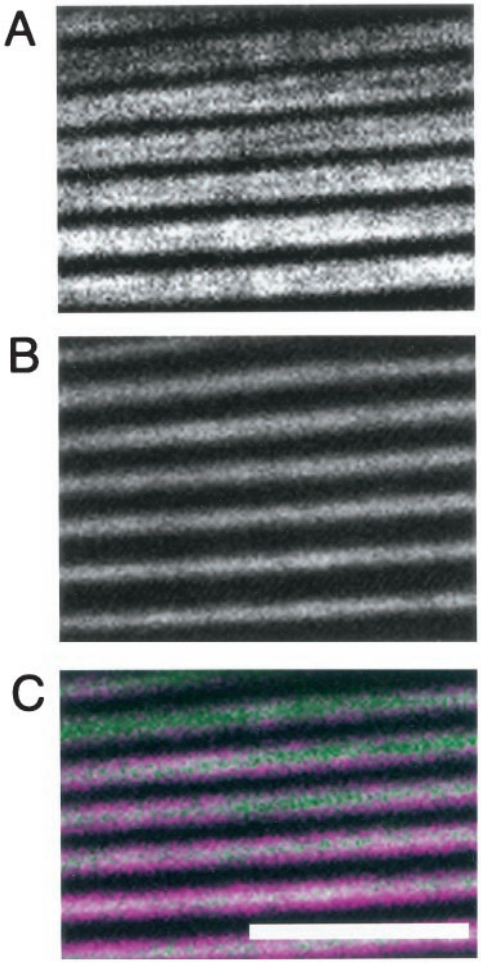

FIGURE 5 Correlative structural localization of the SHG source in nematode myofilament lattice. (*A*) Endogenous SHG and (*B*) TPEF fluorescence from GFP::MHC A in *C. elegans* body wall muscle are shown separately and (*C*) in color overlay (SHG = *violet*, TPEF = *green*). A central green/white stripe in the center of each violet band in (*C*) indicates that GFP::MHC A is localized at the center of the SHG-bright band. Scale bar = 10 μm.

middle portion of the SHG bright band, whereas SHG is strongest in regions not containing GFP::MHC A.

The dim stripe down the center of the bright bands seen in SHG may arise from several causes. First, there is a nonuniform distribution of MHC isoforms along thick filaments in *C. elegans*. The other major isoform in *C. elegans* body wall muscle, MHC B, is known to be restricted to distal portions of thick filaments (Miller et al. 1983; Waterston, 1988). To test whether this isoform was a major contributor to SHG from thick filaments, we imaged a *C. elegans* strain homozygous for a null mutant allele of the gene encoding MHC B, *unc-54(e190)*, that disrupts the sarcomeres. The data are shown in Fig. 6, *A*, *B*, and *C* for the SHG, TPEF, and two-color overlay, respectively. Loss of MHC B resulted in substantial diminution of SHG compared to the wild type, indeed; the laser power needed to be increased to obtain these data. Although irregularly patterned, the source of SHG is still largely spatially distinct from GFP::MHC A. Thus, MHC B contributes significantly to the normal signal, but may do so in combination with both MHC A and paramyosin, the other major coiled-coil component of thick filament outer arms (Epstein et al., 1985; Waterston, 1988).

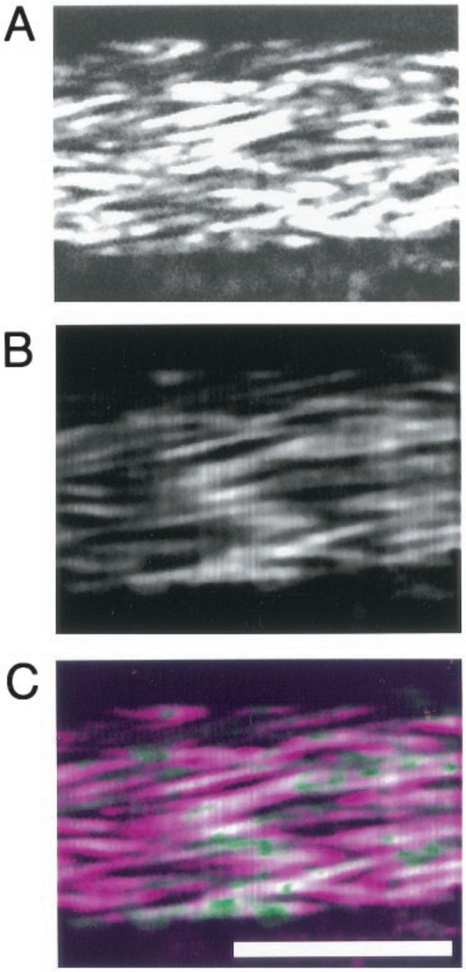

FIGURE 6 Characterization of abnormal myofilament lattice in myosin mutant *C. elegans*. (*A*) Endogenous SHG and (*B*) TPEF fluorescence from GFP::MHC A in body wall muscle of an *unc-54* homozygous mutant *C. elegans* are shown separately and (C*)* in color overlay (SHG = *violet*, TPEF = *green*). Although both signals are structurally associated, the lattice has lost the characteristic order seen in Fig. 5. Note that the SHG signal in this figure required substantially higher laser power than that from the normal muscle shown in Fig. 5 *A*. Scale bar = 10 μm.

Other factors may also explain the dim central stripe. Only the distal portions of the thick filament that comingle and interact directly with actin-based thin filaments may induce SHG. Alternatively, a symmetry-induced cancellation effect (as will also be seen for tubulin structures, below) may arise at the center of the thick filament, where proximal portions of oppositely oriented filament arms are close enough to break down the conditions of local asymmetry required for SHG. This is because SHG is a coherent process, and signals will only arise from objects separated at distances on the order of the optical coherence length, L_c, or larger,

$$\Delta k \cdot L_c \approx \pi, \tag{1}$$

where Δk is the difference in wave vectors between the fundamental and second harmonic waves. This coherence length is material independent and is used to relate the size scale or distance separation over which objects (e.g., beads) that, on a macroscopic scale, are centro-symmetric (or possess inversion symmetry) can produce SHG due to local asymmetries (e.g., each side of a bead). Due to the use of visible or near-infrared laser wavelengths, this effect occurs on approximately the micrometer and submicrometer size scale. For SHG arising from the electric dipole interaction, the lower limit for producing SHG empirically appears to be about $\lambda/10$ (note that electric quadrupole interactions can produce SHG at smaller particle sizes but will not be important for biological samples). At smaller distances, the SHG signals undergo complete destructive interference. This size constraint has recently been well documented in the SHG literature for several samples, including oil droplets, beads, liposomes, cell membranes, and metallic spheres. (Hua and Gersten, 1986; Ostling et al., 1993; Yan et al., 1998; Vance et al.; 1998; Dadap et al., 1999; Campagnola et al., 1999; Moreuax et al., 2000). It should be noted that there are actually two very different operative coherence lengths governing SHG. The other is the material coherence length, which characterizes bulk anisotropies, and, for tissues, is on the order of 20 μm (Kim et al., 1999). For bulk, anisotropic materials, SHG arises from constructive interference within this length and drops off for larger lengths. Note that the maximum material coherence length will not be reached on a laser-scanning nonlinear microscope.

Tubulin

Birefringence is characteristic of microtubule-based structures and myofilaments (Cassimeris et al., 1988). To test whether the second harmonic could also be generated within complexes that are not composed of coiled-coil structures, we imaged tubulin structures in *C. elegans* embryos by SHIM. To examine the specific contexts giving rise to SHG from microtubules, we imaged by simultaneous SHG/TPEF a strain of *C. elegans* expressing a GFP-tagged β tubulin (β-tubulin::GFP). In Fig. 7, *A*, *B*, and *C*, the SHG, TPEF, and overlay, respectively, show a gravid adult hermaphrodite bearing eight embryos within its uterus. SHG signal was detected from tubulin arrays at all cell-cycle stages, including pronuclear rotation in the zygote (*far left*), mitosis in the first cell division (*far right*), interphase in the two-cell stage (*second from left*), and various later phases of early embryonic cleavage. However, at high magnification, it was clear that SHG arises from only a subset of the microtubules seen by TPEF. In Fig. 8, *A*, *B*, and *C*, the SHG, TPEF, and overlay, respectively, show an embryo during the first mitosis. Fluorescent microtubules compose the dense spindle array and sparse astral arrays surrounding both spindle poles (Fig. 8, *B* and *C*). Yet SHG within the spindle (Fig. 8, *A* and *C*) is interrupted by a discrete dark space at the spindle midzone, and the spindle poles appear distinctly more hollow by SHG than by TPEF. In Fig. 9, *A–C*, two interphase centrosomes in early embryonic cells are shown. Although, centrosomes are uniformly labeled with fluorescent tubulin (Fig. 9 *B*), they yield hollow double-crescent SHG profiles

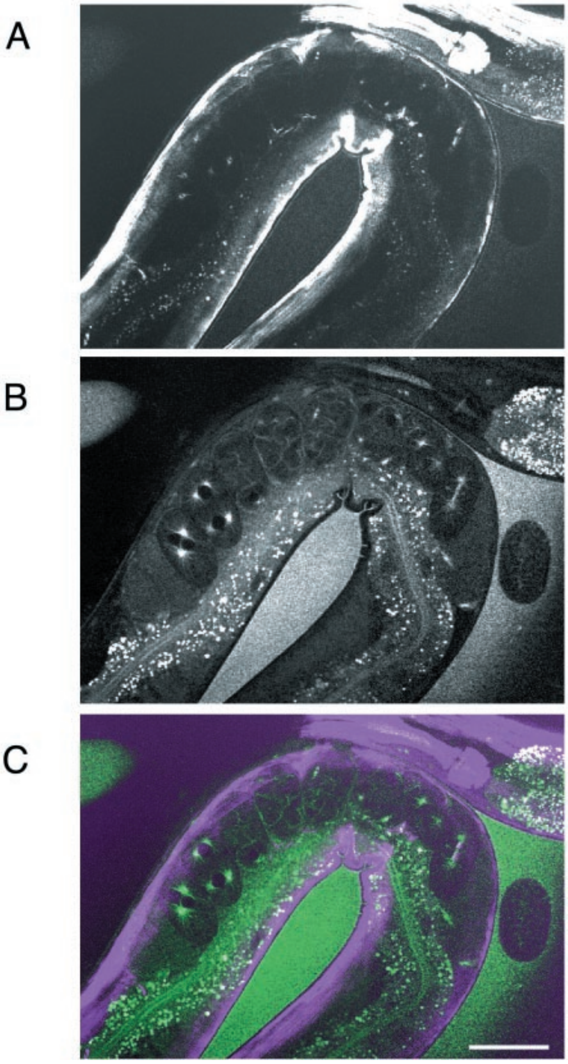

FIGURE 7 SHG from tubulin structures in *C. elegans* embryos. (*A*) SHG and (*B*) TPEF, and (*C*) color-overlay optical section taken through early embryos within the uterus of live *C. elegans* allow comparison between signal profiles for the two imaging modes. Eight embryos are shown within the uterus of an adult worm at low magnification. Stages seen include pronuclear rotation in the zygote (*far left*), mitosis in the first cell division (*far right*), interphase in the two-cell stage (*second from left*), and various stages of early embryonic cleavage. Scale bar = 50 μm.

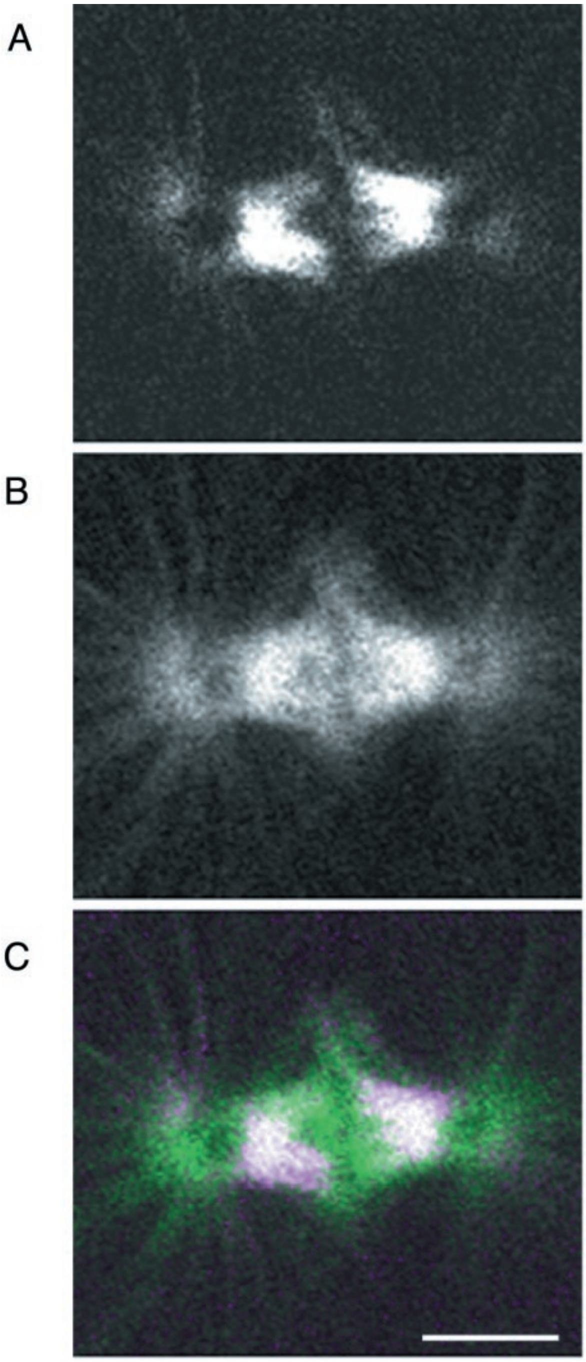

FIGURE 8 (*A*) SHG, (*B*) TPEF, and (*C*) color overlay of an embryo shown at higher magnification during the first mitosis. In (*B*), fluorescent microtubules compose the dense spindle array and sparse astral arrays surrounding both spindle poles. In (*A*), however, SHG arises from only a subset of the microtubules seen in (*B*); bright SHG in the spindle is interrupted by a discrete dark space at the spindle midzone; only proximal portions of a few astral microtubule bundles are seen; and the spindle poles appear distinctly more hollow by SHG than by TPEF. Scale bar = 10 μm.

(Fig. 9, *A* and *C*). In contrast, SHG-bright autofluorescent granules in the intestine of the mother are uniform (Fig. 9, *A* and *C*, *arrows*). It should be noted that wild-type worms

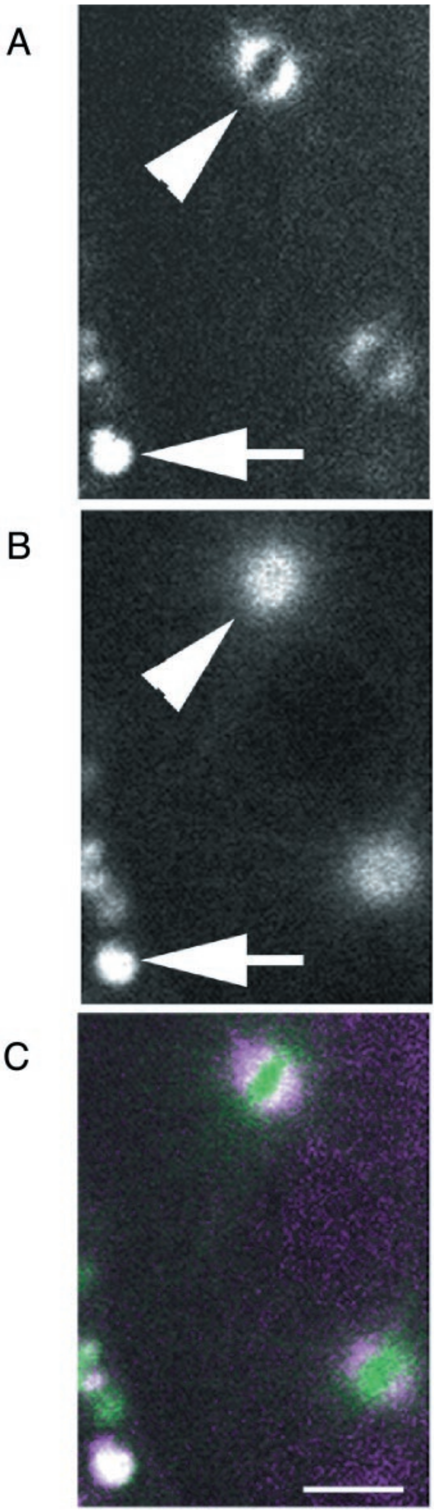

FIGURE 9 (*A*) SHG, (*B*) TPEF, and (*C*) color overlay of two interphase centrosomes in early embryonic cells are shown at high magnification (*arrowheads* in *A* and *B*). In (*B*), centrosomes are uniformly labeled with fluorescent tubulin. In (*A*), centrosomes yield hollow SHG profiles, with an angular dependence on the coronal brightness. In contrast, SHG-bright granules in the intestine of the mother are uniform (*arrows*). Scale bar = 10 μm.

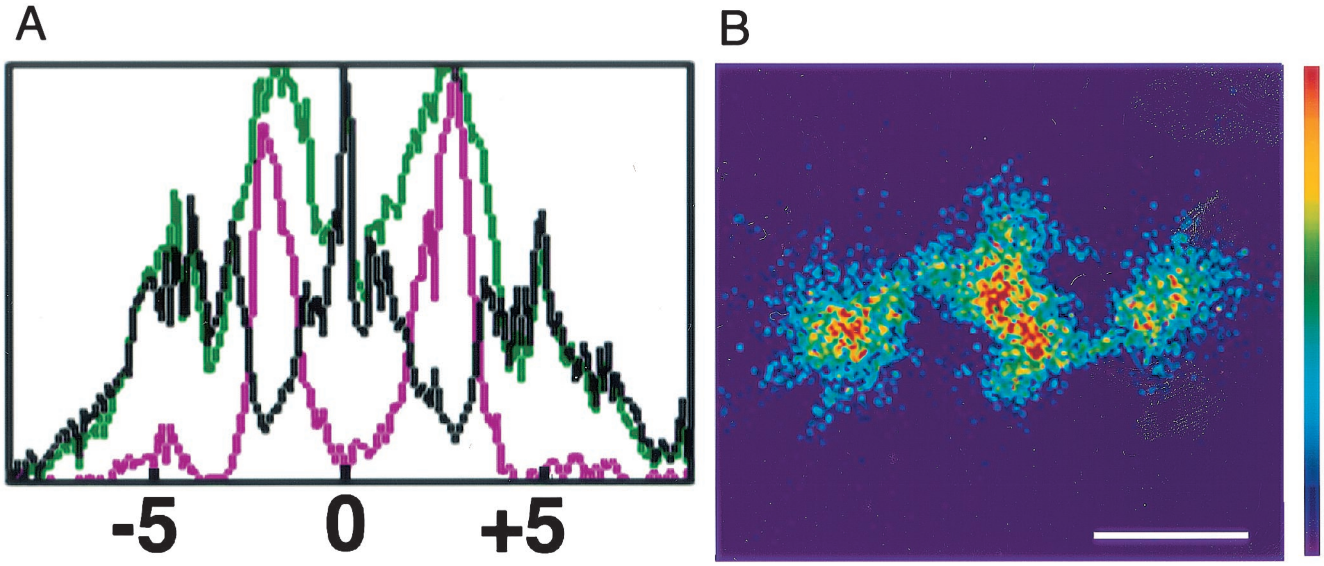

FIGURE 10 Correlation between SHG and TPEF tubulin signals by ratio imaging. (*A*) Self-normalized plots of SHG (*violet*), TPEF (*green*), and TPEF/SHG (*black*) along the length of the spindle shown in Fig. 8. (*B*) A TPEF/SHG ratio image of the data from Fig. 8. Pseudocolor intensity scale for (*B*) is shown to the right. Scale bar = 10 μm.

produced comparable SHG images of asters and spindles (not shown), proving that SHG only arises from the endogenous microtubules and does not arise from the GFP. Two important dependencies of SHG upon orientation are manifested in the signal from tubulin. First, when using a linearly polarized laser source, second harmonic waves will only be produced by the subset of molecules whose dipoles are aligned with the laser polarization. Because microtubules are radially arrayed around the organizing center, the intensity of the SHG signal varies around the centrosome with the coincidence of the laser polarization and the orientation of the microtubules, giving rise to the observed crescents (Fig. 9, *A* and *C*). Second, because SHG is a coherent process, oppositely oriented second harmonic waves produced by oppositely oriented protein structures destructively interfere within a distance less than the optical coherence length ($\sim\lambda = 860$ nm). In the spindle midzone, the microtubules interdigitate counter-parallel to each other (Haimo, 1985; Euteneuer and McIntosh, 1980). Therefore, these regions may appear dark by SHG (Fig. 8, *A* and *C*) because of symmetry cancellation even though they contain abundant microtubules, as evidenced in the TPEF images (Fig. 8, *B* and *C*).

Thus, important information about the structural context of chromophoric molecules is encoded in their SHG signal, and is best comprehended in comparison to a structure-independent imaging mode, such as TPEF from a flexibly tethered GFP domain. Because both nonlinear effects occur at precisely the same point of laser focus, the separate data channels collected are absolutely contemporaneous and colocalized. Figure 10 shows intensity plots along the axis of the spindle shown in Fig. 8. Traces are drawn for the separate SHG and TPEF channels and for the TPEF/SHG ratio. In both representations, the ratio signal is clearly maximized (i.e., strong fluorescence with weak SHG) in zones of high microtubule overlap or symmetry. Therefore, the combination of these modalities is well suited to a ratio-imaging scheme revealing structural detail that is invisible by either mode alone and otherwise apparent only via electron microscopy. This ability to infer molecular context by correlation of multimode imaging profiles has also been recently demonstrated for simultaneous SHG/TPEF imaging of contrast-generating dyes within giant unilamellar vesicles (Moreaux, et al., 2000, 2001).

Optical experiments confirming and characterizing SHG emission

Physical description

In general, the total polarization for a material can be expressed as

$$P = \chi^{(1)}E^1 + \chi^{(2)}E^2 + \chi^{(3)}E^3 + \cdots, \qquad (2)$$

where P is the induced polarization, $\chi^{(n)}$ is the nth-order nonlinear susceptibility tensor, and E is the electric field vector. The first term describes normal absorption and reflection of light; the second term, SHG, sum and difference frequency generation; and the third term, two-photon absorption, third-harmonic generation, and stimulated Raman processes. SHG is a second-order nonlinear optical process that can only arise from media lacking a center of symmetry. This criterion can be satisfied at interfaces and by anisotropic crystals. The second-harmonic intensities per laser pulse are expected to scale as (Shen, 1989)

$$SHG_{\mathrm{sig}} \propto \left[\frac{p}{a\tau}\right]^2 \tau(\chi^2)^2 a, \tag{3}$$

where p is the pulse energy, a is the area of the focused spot, χ^2 is the second-order nonlinear susceptibility of the protein, and τ is the laser pulse width. The inverse dependence on the pulse width arises because, although the signal scales as the square of the peak power, second harmonic will only be produced within the duration of the laser fundamental pulse. Note that SHG and two-photon excitation probabilities have the same inverse pulse width dependence. Similarly, because the signal is proportional to the square of the intensity (photons/area), second harmonic will only be generated within the focal area. The squared dependence of χ^2 on the signal magnitude is manifested in a squared dependence of the molecular concentration.

Several control measurements were performed to verify that the SHG images only consisted of the second harmonic and no residual laser light or autofluoresence. First, the laser was taken out of mode locking and the signals vanished, indicating that the signals arose from a nonlinear process, which was also verified by a quadratic dependence on the laser power (data not shown). To show that the images were free of autofluorescence, SHG spectra of all the specimens were collected using a fiber-based spectrometer. The data for 850-nm excitation for five specimens are shown in Fig. 11 and clearly shows that the signal arose exclusively at the expected 425-nm wavelength, without any autofluorescence. Further, all the spectra have the same bandwidth (~10 nm), and this width is consistent with the expectation for 100-fs pulses: a Fourier transform-limited 100-fs pulse will have a full-width half-maximum (FWHM) bandwidth of ~10 nm, and, for a Gaussian beam, the second harmonic will have a FWHM of $1/\sqrt{2}$ of the fundamental or ~7 nm. Within experimental limitations (spectrometer resolution and nontransform limited pulses), the observed value is in good agreement with that predicted. Next, the laser was scanned between 820 and 880 nm to ensure that the SHG spectrum tracked with the excitation wavelength, and the resulting spectra are shown in Fig. 12. Note that the corresponding SHG wavelengths are the only wavelengths efficiently passed by the 425-nm hard reflector in the beam path after the condenser. The spectra do indeed follow the excitation with the proper bandwidth, and are again free of any autofluorescent contamination. Finally, the transmitted light was dispersed through a 0.25-m monochromator and then imaged. Although this scheme is very inefficient as the laser is scanning, images were obtained from both a fishscale and adult *C. elegans*. If uncontaminated by autofluorescence, the SHG signal should only be present at half the laser fundamental wavelength, and then tune when the laser fundamental is scanned. Measurements were taken at fundamental wavelengths of 800, 845, and 885 nm, and, indeed, the SHG did tune accordingly. Additionally, a bound was placed on the extent of autofluorescence occurring within this spectral window. With the laser fundamental at 840 nm, the SHG image was obtained at 420 nm. Then the laser was tuned to 860 nm, and the corresponding image was obtained at 420 nm. Following background subtraction, the ratio of the intensities of these two images places an upper bound on autofluorescence in the fish scale, where a value of 1:500 was obtained. Finally, the SHG image appeared bleach resistant, and data will be presented in a latter section to provide quantitative evidence of this observation.

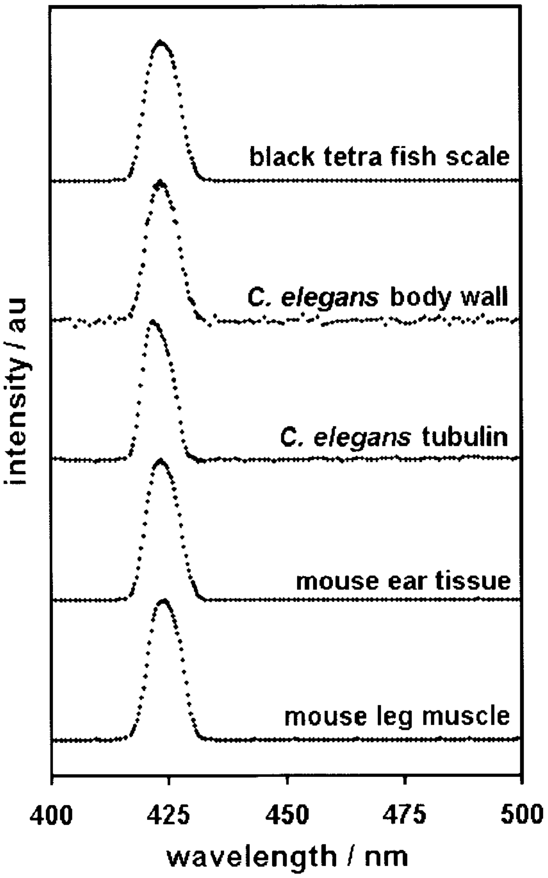

FIGURE 11 SHG spectra for the species used in this work. The laser excitation wavelength was 850 nm. The spectra are free of any contaminating autofluorescence.

Polarization anisotropy

An additional aspect of SHIM is the capability of probing the orientation of structural proteins in tissues. The vector nature can be exploited to provide data on the spatial organization, i.e., long-range order, of the helices from the size range of 500 nm and larger by using SHG polarization

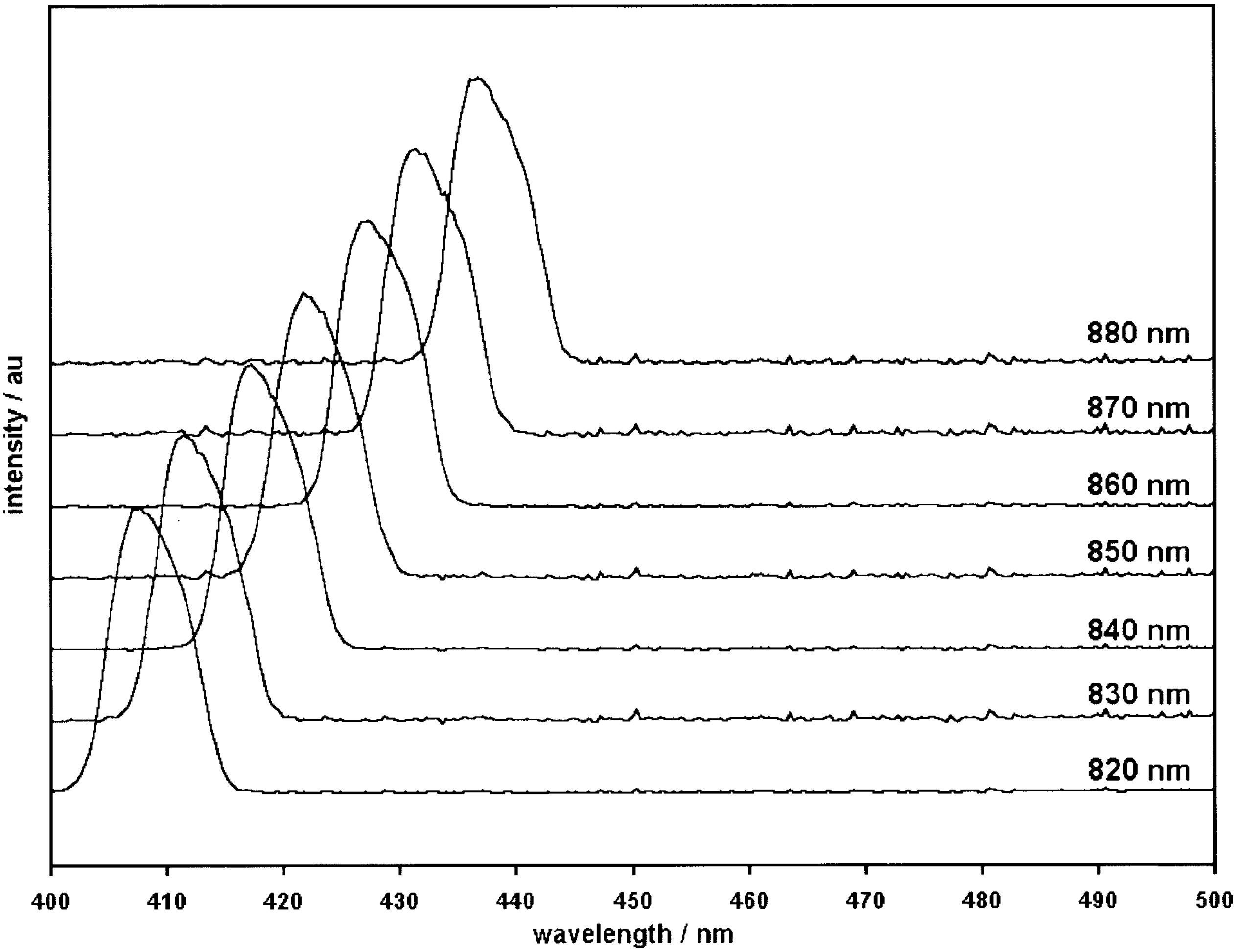

FIGURE 12 SHG spectra of pharyngeal muscle of *C. elegans* tracks the excitation wavelength over the range of 820–880 nm. The spectra are all normalized to the same maximum value. No contaminating autofluorescence is observed in this spectral range.

anisotropy measurements. This is analogous to the more familiar fluorescence anisotropy to probe organized structures, however the SHG approach is somewhat more specific and does not require exogenous labels. For processes arising from an electric dipole process (e.g., absorption, and SHG), the angular distribution of excitation is given by the second Legendre polynomial (a $\cos^2$ function). The anisotropy parameter, β, describing the molecular orientation, is derived from this function, and, when using linearly polarized light, is given by

$$\beta = \frac{I_{\mathrm{par}} - I_{\mathrm{perp}}}{I_{\mathrm{par}} + 2I_{\mathrm{perp}}}, \tag{4}$$

where I_{par} and I_{perp} are the intensities of the signals whose polarizations are parallel and perpendicular to the polarization of the incident laser. This parameter can vary between -0.5, and 1. The special case of 0 represents the isotropic situation where I_{par} and I_{perp} are equal and would physically correspond to having complete randomization or disruption of the helices. The value of 1 would correspond to complete ordering relative to the incident laser, i.e., having well-aligned, well structured helices. Images acquired from collagen in a fish scale with the output polarization oriented parallel and perpendicular to the excitation laser are shown in Fig. 13, *A* and *B*, respectively. Integrating these data yields a β value of 0.7. The actual value is probably somewhat closer to unity because the use of medium or high numerical objective lenses results in a slight loss of polarization (Axelrod, 1979). This result indicates the highly ordered nature of the collagen fibrils. Note that the use of the appropriate combinations of input laser polarization and output polarization analysis will also yield the absolute molecular orientations by determining the value of all the contributing matrix elements of the second-order nonlinear susceptibility tensor (Shen, 1989).

Molecular symmetry can also be observed by rotating the input laser polarization and collecting the resulting SHG signal. SHG images of interphase centrosomes from early

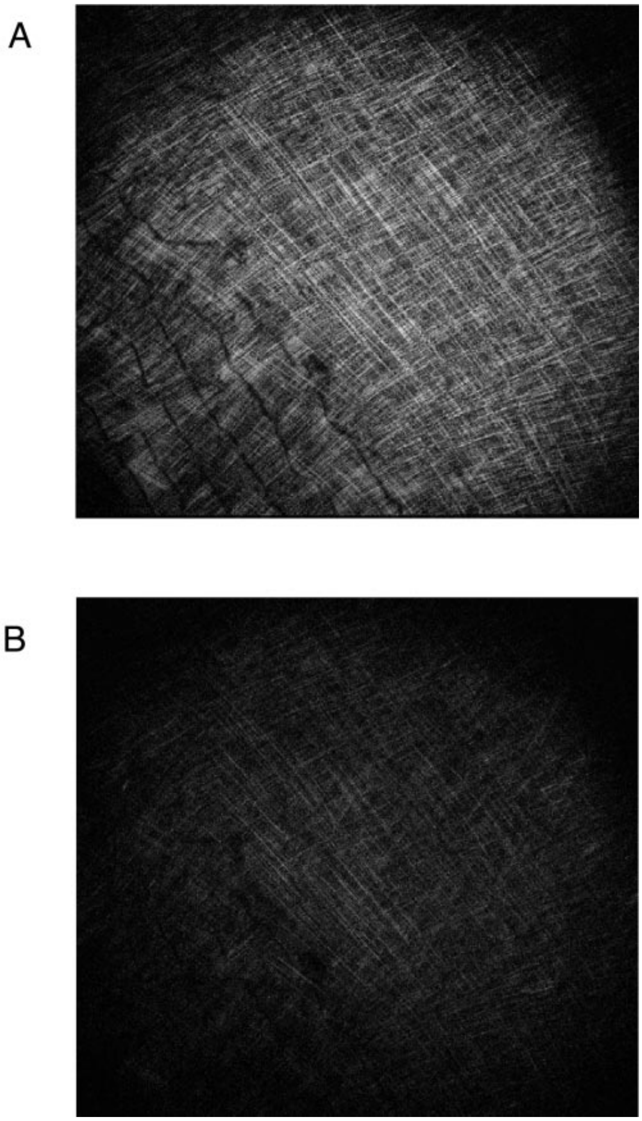

FIGURE 13 SHG polarization anisotropy measurements of an isolated scale of black tetra fish, *G. ternetzi*, from the Glan Laser polarizer oriented (*A*) parallel and (*B*) perpendicular to the laser fundamental.

C. elegans embryos are shown in Fig. 14, where the data in *A*, *B*, and *C* were collected from the same sets of centrosomes with varying excitation polarization obtained by rotation of a wave plate. The rotation of the crescents follows all the way through 90°, showing that the interaction of the laser with the radial symmetry of the microtubule array strongly influences the image contrast. Note that it would be predicted that the use of circularly polarized light would equally excite all orientations and result in continuous circles of constant intensity. In our current geometry, we were unable to achieve this condition because substantial ellipticity is introduced in the galvo scanning system due to the non-normal angles of incidence and the metal mirror coatings. The use of a full wave plate following the scanner would eliminate this residual ellipticity.

DISCUSSION

Physical origin of SHG in tissues

SHG relies on the lack of inversion symmetry, and this condition can be satisfied in several ways, including the molecular alignment in a crystal or the intrinsic asymmetry at an interface. In prior work, we exploited the fact that the plasma membrane in a cell provides a biological liquid–liquid interface, and that high resolution images of living cells could be obtained when this membrane was stained with a contrast- increasing dye (Ben-Oren et al., 1996; Peleg et al., 1999; Campagnola et al., 1999). The work presented here is fundamentally different in that the contrast does not arise from cell membranes but rather from endogenous structural proteins present in tissue. From polarization microscopy, muscle and connective tissues are known to be highly birefringent. However, an analogy cannot be directly drawn to frequency doubling in a birefringent uni-axial crystal, such as KDP or BBO. In such crystals, the laser fundamental and resulting SHG waves have orthogonal polarizations, because this is the only nonvanishing matrix element of $\chi^{(2)}$ (Yariv, 1989). However, we measured the polarization anisotropy of the SHG signal both parallel and perpendicular to the laser fundamental in both fish scales and *C. elegans* muscle and found the SHG signals in both cases were strongly polarized parallel to the fundamental (see Fig. 13). Furthermore, no Type 1 phase-matching condition exists for these proteins at these wavelengths (Bolin et al., 1989). However, phase-matching requirements are not rigorously applicable for the case of strongly focused Gaussian beams. In their 1986 work, Freund et al. showed that the collagen from rat tail tendon had dipolar structures that gave rise to the SHG signals. Our data from the tubulin structures (Fig. 7–10, 14) are consistent with the SHG arising from an electric dipole interaction. However, these structural proteins are all intrinsically chiral, and chirality is known to enhance SHG. This has been shown recently by Hicks and coworkers (Beyers et al., 1994) for chiral molecules at an interface and in our prior work comparing the SHG efficiencies of chiral and nonchiral dyes (Campagnola et al., 1999). This concept was also demonstrated by Verbiest et al. (1998) in studying SHG in synthetic helicenes. They showed that, although racemic mixtures of the chiral helicenes did produce second harmonic signals, the pure enantiomers were upwards of 50-fold more efficient. Note that, although chirality alone can give rise to SHG, this process is inefficient and would lead to isotropic angular distributions. This is in strong contrast to the strongly anisotropic data on fish scale collagen and *C. elegans* centrosome asters shown in Figs. 13 and 14, respectively. Thus, the SHG can be ascribed to a dipolar process that is chirality enhanced, where the signal arises from a volume rather than surface effect. A direct analogy can be drawn from the results in helicenes (Verbiest et al., 1998) to the work here on endogenous proteins. The brightest signals were from the

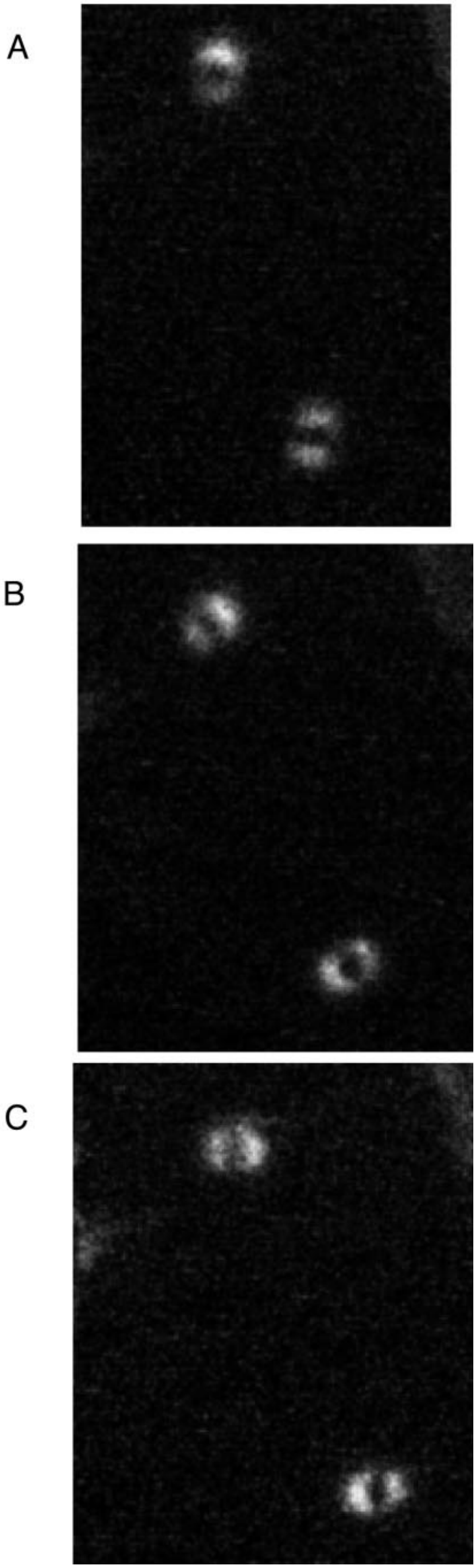

fish scale and mouse ECM, where, in both cases, the signal arose from a collagen matrix and were considerably brighter than either the mouse or *C. elegans* sarcomeres. The coiled-coils in collagen, for example, will display supra-molecular chirality, i.e., although each of individual helices in the triple-helical collagen structure is expected to produce second-harmonic signals, the three helices will cooperatively produce even larger signals. By contrast, myosin has two coiled-coils and would be expected to be less SHG efficient. This is consistent with work by Kim et al. (1999, 2000), where, in bulk measurements (nonimaging), they compared relative efficiencies of several forms of connective tissue and muscle tissue and found ratios in the range of 50/1.

The signal strengths observed from the structural proteins in this work are much greater, ~10–50 fold, than were obtained in our prior work on imaging cellular membranes stained with a voltage-sensitive dye. This is an interesting result in that it is expected that the molecular hyperpolarizability for a highly polarizable dye will be much greater than that of a protein. This is because highly conjugated pi systems, in general, lead to greater second-order properties (Tykwinski et al., 1998), and proteins lack such extended pi networks. For example, collagen typically has a sparse density of aromatic residues and the polarizability of single bonds is significantly less than that of double bonds. Even more so, our prior SHG imaging work (Campagnola et al., 1999) was done on resonance to provide sufficient contrast where the resonant component was at least an order of magnitude larger than the pure surface term. By contrast, the apparent lack of spectral dependence on the signal levels from these structural proteins indicates that there is little resonance enhancement in any of these images. However, myosin and collagen probably occur in millimolar abundance, whereas cellular membranes can only be stained in the 1–10 μM level to avoid aggregation and toxicity. Thus the quadratic dependence of the second-harmonic signals on concentration leads to unexpectantly intense images from structural proteins.

Symmetry effects on SHG

We showed the effects of both radial and lateral symmetry on the SHG images of tubulin structures in *C. elegans*. It is interesting to compare this to the fluorescent image arising from β-tubulin::GFP. In Fig. 8, SHG is excluded from the center of the spindle midzone, where GFP-labeled microtubules are abundant but an anti-parallel arrangement of microtubules exists, in contrast to more harmonogenic distal

FIGURE 14 SHG images of *C. elegans* early embryo centrosomes (similar to Fig. 10), where the polarization was effectively rotated with a quarter-wave plate, where (*A*) and (*C*) were the result of 45° of plate rotation (i.e., 90° optical rotation), resulting in orthogonal projections of the array; and (*B*) was no rotation.

portions of the spindle. The centrosomal region of both spindle poles and asters is also devoid of SHG signal, even when microtubule density appears highest there by fluorescence (Fig. 9). The centrosome is characterized by a 3D radially symmetric array of microtubules in close proximity. Cylindrical symmetry cancellation is not observed in the TPEF channel because the GFP domain is flexibly tethered to the tubulin domain. Thus, because of the lack of rigidity, it is expected to be randomly oriented and generate fluorescence at all polarization angles. Similarly, the interdigitated counter-parallel GFP-labeled microtubules produce strong fluorescence in the midzone. Because fluorescence is an incoherent process, it is not subject to the distance constraints that SHG experiences within the optical coherence length.

Comparison with other forms of microscopy

Second-harmonic imaging of tissues has distinct advantages over imaging specimens stained with fluorescent dyes. The most obvious advantage lies in the lack of any staining preparation. Extensive processing—fixation, staining, sectioning—is typically required to image the fine 3D structure of complex biological specimens. Similarly, there are no cytotoxic or phototoxic effects from the addition of exogenous labels. Bleaching of fluorescent dyes results in the creation of toxic free radicals, and, although multiphoton excitation of fluorescence greatly reduces this problem away from the focal plane, in-plane excitation will still result in phototoxicity, and limit studying dynamics over long time courses or limit repeat acquisition to increase signal-to-noise and image quality. It should be noted that, at the wavelengths used (~850 nm), there is no apparent resonant component of the SHG arising from these structural proteins by either two- or three-photon absorption, as evidenced by the lack of clear spectral dependence. To further verify this lack of photobleaching, we irradiated *C. elegans* adults expressing GFP::MHC A construct at high zoom with high laser power over several scans. The data are shown in Fig. 15, where low zoom images were obtained before and after irradiation at high zoom. The darkened rectangle in the TPEF channel (*B*) arises from photo-bleaching the GFP, whereas the SHG image (*A*) is unaffected, confirming the bleach-free nature of SHG signal.

The use of both GFP and highly selective chemical fluorescent probes has added new dimensions to the capabilities of imaging live cells. However, genetically engineered expression or chemical administration of fluorescent labels can be a major limiting step in studies of nonmodel organisms. Because SHIM takes advantage of signals generated by endogenous structures, it should be universally applicable to all animal species, and is perhaps ideally suited for development of medical imaging strategies. We have shown here that a wide range of proteins in several tissue types is readily visualized by SHIM without the effort of exogenous labeling. Furthermore, because SHG arises within the endogenous proteins of interest, it encodes information on molecular orientation and assembly that cannot be elicited from the fluorescence of GFP-labeled variants (see Figs. 9 and 10). GFP is typically tethered to the end of a domain, with a pronounced lack of rigidity, and hence cannot provide information on molecular-level orientation and structure. This is because the GFP will be freely rotating and the fluorescence polarization anisotropy will become isotropic. Similarly, information regarding both radial and lateral symmetry will be lost.

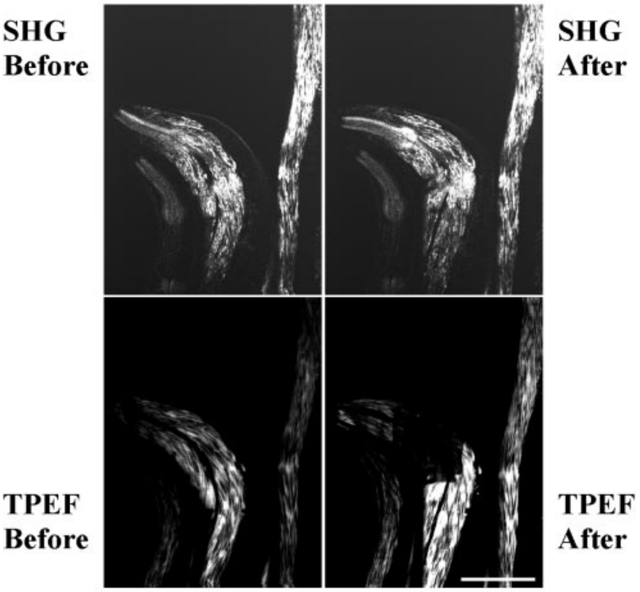

FIGURE 15 SHG signal is not subject to photobleaching, demonstrated using the same *C. elegans* strain shown in Fig. 5. Top and bottom panels are SHG and TPE fluorescence of GFP, respectively, before (*left*) and after (*right*) high-intensity, high-zoom scanning of a central portion of the field. The SHG is unaffected whereas the GFP fluorescence is strongly bleached after exposure at high zoom. Scale bar = 50 μm.

Because it has been known for some time from polarization microscopy that structural proteins organize to form highly birefringent structures (Inoue, 1986), it is useful to compare the data obtained by SHIM with that from polarization microscopy. As shown in the Results section (Fig. 4), while the images from these two modalities may appear similar, there are significant differences in the method of contrast generation. Polarization images probe linear birefringence and can only achieve contrast by having orthogonal polarizers for excitation and collection. Thus, it is difficult to obtain absolute orientation of molecules. By contrast, SHG signals can be acquired for arbitrary output polarizations relative to the excitation laser, and both relative and absolute molecular orientations can be obtained through the proper choice of input and output polarizations (Shen, 1989). Additionally, it is possible to estimate the width of a distribution of orientations through this analysis.

Finally, because of the nonlinear nature, SHIM provides intrinsic optical sectioning, whereas this is difficult by polarization microscopy. This feature is especially important in imaging whole tissue samples and extending this scheme to in vivo specimens.

Limits on data acquisition

The data-acquisition rate here was typically 1 frame per second, each frame consisting of 768 × 512 pixels. This was generally limited by the scanner speed rather than image intensity. With a different experimental arrangement, line scans could be acquired to obtain images on physiological time scales. Alternatively, much faster frame rates could be realized with a resonant galvo scanner system. The depth of imaging through thick tissue is limited by the Rayleigh scattering of both the fundamental and SHG waves. We have readily achieved depths of >500 μm through muscle tissue.

CONCLUSIONS

Our results demonstrate that SHIM, alone and in combination with TPEF, offers novel opportunities for analyses of endogenous protein polymer structure within living, 3D specimens. The simultaneous imaging of SHG and two-photon excited GFP enhances our understanding of the protein species and structural contexts giving rise to the second-harmonic signal. Polarization analyses can yield data regarding the molecular organization and symmetry of these matrices. We expect that these methods will have significant impact on in vivo studies in various fields of biology, including tissue organization, wound-healing, myofilament assembly, muscle development and disease, and the division cycle of normal and cancerous cells in situ. Already, we have begun to extend these methods to the analysis of fibrillar species in connective tissue and studies of skin and muscle pathology.

We gratefully acknowledge financial support under the National Science Foundation Academic Research Infrastructure DBI-9601609, the State of Connecticut Critical Technology program, and National Institutes of Health R01- GM35063 (to A.C.M.). This work was also supported by a New Scholar in Aging grant from the Ellison Medical Foundation and a Research grant from the Muscular Dystrophy Association to W.A.M., National Institute of General Medical Sciences grant R01-GM60389 to M.T.

We thank Prof. Vladimir Rodionov for providing the fish scales, Prof. David Rowe and Ivo Kalajzic for mouse tissues, and Prof. Andrew Z. Fire for gifts of DNA. We also thank Prof. Leslie Loew, Prof. John White, and Prof. Ann Cowan for helpful technical discussions.

REFERENCES

Axelrod, D. 1979. Carbocyanine dye orientation in red cell membrane studied by microscopic fluorescence polarization. *Biophys. J.* 26: 557–573.

Ben-Oren, I., G. Peleg, A. Lewis, B. Minke, and L. Loew. 1996. Infrared nonlinear optical measurements of membrane potential in photoreceptor cells. *Biophys. J.* 71:1616–1620.

Beyers, J. D., H. I. Lee, T. Petralli-Mallow, and J. M. Hicks. 1994. Second-harmonic generation circular-dichroism spectroscopy from chiral monolayers. *Phys. Rev. B.* 49:14643–14647.

Bloembergen, N., R. K. Chang, S. S. Jha, and C. H. Lee. 1968. Optical second-harmonic generation in reflection from media with inversion symmetry. *Phys. Rev.* 174:19813–19822.

Bolin, F. P., L. E. Preuss, R. C. Taylor, and R. J. Ference. 1989. Refractive index of some mammalian tissue using a fiber optic cladding method. *Appl. Opt.* 28:2297–2303.

Campagnola, P. J., M. D. Wei, A. Lewis, and L. M. Loew. 1999. High resolution non-linear optical microscopy of living cells by second harmonic generation. *Biophys. J.* 77:3341–3349.

Cassimeris, L., S. Inoue, and E. D. Salmon. 1988. Microtubule dynamics in the chromosomal spindle fiber: analysis by fluorescence and high-resolution polarization microscopy. *Cell Motil. Cytoskel.* 10:185–196.

Dadap, J. I., Shan, K. B. Eisenthal, and T. F. Heinz. 1999. Second-harmonic Rayleigh scattering from a sphere of centrosymmetric material. *Phys. Rev. Lett.* 83:4045–4048.

Denk, W., J. H. Strickler, and, W. W. Webb. 1990. Two-photon laser scanning fluorescence microscopy. *Science.* 248:73–76.

Eisenthal, K. B. 1996. Liquid interfaces probed by second-harmonic and sum-frequency spectroscopy. *Chem. Rev.* 96:1343–1360.

Epstein, H. F., D. M. Miller, III, L. A. Gossett, I. Ortiz, and G. C. Berliner. 1985. Myosin and paramyosin are organized about a newly identified core structure. *J. Cell Biol.* 100:904–915.

Euteneuer, U., and J. McIntosh. 1980. Polarity of midbody and phragmoplast microtubules. *J. Cell Biol* 87:509–515.

Freund, I., M. Deutsch, and A. Sprecher. 1986. Connective tissue polarity. *Biophys. J.* 50:693–712.

Gauderon, R., P. B. Lukins, and C. J. R. Sheppard. 1998. Three-dimensional second harmonic generation imaging with femtosecond laser pulses. *Optics Lett.* 23:1209–1211.

Guo, Y., P. P. Ho, H. Savage, D. Harris, P. Sacks, S. Schantz, F. Liu, N. Zhadin, and, R. R. Alfano. 1997. Second-harmonic tomography of tissues. *Optics Lett.* 22:1323–1325.

Guo, Y., H. Savage, F. Liu, N. Zhadin, S. Schantz, P. P. Ho and, R. R. Alfano. 1999. Subsurface tumor progression investigated by noninvasive second-harmonic tomography. *Proc. Natl. Acad. Sci. U.S.A.* 96: 10854–10856.

Haimo, L. 1985. Microtubule polarity in taxol-treated isolated spindles. *Can. J. Biochem. Cell Biol.* 63:519–532.

Hellwarth, R., and P. Christensen. 1974. Nonlinear optical microscopic examination of structure in polycrystalline ZnSe. *Optics Comm.* 12: 318–322.

Hoppe, P. E., and R. H. Waterston. 1996. Hydrophobicity variations along the surface of the coiled-coil rod may mediate striated muscle myosin assembly in *Caenorhabditis elegans*. *J. Cell Biol.* 135:371–382.

Hua, X. M., and J. I. Gersten. 1986. Theory of second-harmonic generation by small metal spheres. *Phys. Rev. B.* 33:3756–3764.

Inoue, S. 1986. An introduction to biological polarization microscopy. *In* Video Microscopy. Plenum Press, NY. 477–510.

Kim, B.-M., J. Eichler, and L. B. Da Silva. 1999. Frequency doubling of ultrashort laser pulses in biological tissue. *Appl. Opt.* 38:7145–7150.

Kim, B.-M., J. Eichler, K. M. Reiser, A. M. Rubinchik, and L. B. Da Silva. 2000. Collagen structure and nonlinear susceptibility: effects of heat, glycation, and enzymatic cleavage on second harmonic generation signal intensity. *Lasers Surg. Med.* 27:329–335.

Kleinman, D. A. 1962. Nonlinear dielectric polarization in optical media. *Phys. Rev.* 126:1977–1979.

Mello, C. C., J. M. Kramer, D. Stinchcomb, and V. Ambros. 1991. Efficient gene transfer in *C. elegans*: extrachromosomal maintenance and integration of transforming sequences. *EMBO J.* 10:3959–3970.

Miller, D. M., I. Ortiz, G. C. Berliner, and H. F. Epstein. 1983. Differential localization of two myosins within nematode thick filaments. *Cell.* 34:477–490.

Moreaux, L., O. Sandre, M. Blanchard-Desce, and J. Mertz. 2000. Membrane imaging by simultaneous second-harmonic generation and two-photo microscopy. *Optics Lett.* 25:320–322.

Moreaux, L., O. Sandre, S. Charpak, M. Blanchard-Desce, and J. Mertz. 2001. Coherent scattering in multi-harmonic light microscopy. *Biophys. J.* 80:1568–1574.

Ostling, D., P. Stampfli, and K. H. Bennemann. 1983. Theory of nonlinear properties of small metallic spheres *Z. Phys. D.* 28:169–175.

Peleg, G., A. Lewis, M. Linial, and L. M. Loew. 1999. Non-linear optical measurement of membrane potential around single molecules at selected cellular sites. *Proc. Natl. Acad. Sci. U.S.A.* 96:6700–6704.

Shen, Y. R. 1989. Surface properties probed by second-harmonic and sum-frequency generation. *Nature.* 337:519–525.

Sheppard, C. J. R., R. Kompfner, J. Gannaway, and D. Walsh. 1977. Scanning harmonic optical microscope. *IEEE J. Quantum Electron.* 13E:100D

Strome, S., J. Powers, M. Dunn, K. Reese, C. J. Malone, J. White, G. Seydoux, and, W. Saxton. 2001. Spindle dynamics and the role of γ-tubulin in early *C. elegans* embryos. *Mol. Biol. Cell.* 12:1751–1764.

Tykwinski, R. R., U. Gubler, R. E. Martin, F. Diederich, C. Bosshard, and P. Gunter. 1998. Structure–property relationships in third-order nonlinear optical chromophores. *J. Phys. Chem. B.* 102:4451–4465.

Vance, F. W., B. I. Lemon, and J. T. Hupp. 1998. Enormous hyper-Rayleigh scattering from nanocrystalline gold particles suspensions. *J. Phys. Chem. B.* 102:10091–10093.

Verbiest, T., S. V. Elshocht, M. Kauranen, L. Hellemans, J. Snauwaert, C. Nuckolls, T. J. Katz, and A. Persoons. 1998. Strong enhancement of nonlinear optical properties through supramolecular chirality. *Science.* 282:913–915.

Waterston, R. H. 1988. Muscle. *In* The Nematode *Caenorhabaditis elegans*. W. B. Wood, editor. Cold Spring Harbor Laboratory, Cold Spring Harbor, NY. 281–335.

Yariv, A. 1989. Introduction to non-linear optics—second-harmonic generation. *In* Quantum Electronics. Wiley, New York. 378–406.

Yan, C. Y., Y. Liu, and K. B. Eisenthal. 1998. New method for determination of surface potential of microscopic particles by second harmonic generation. *J. Phys. Chem. B.*102:6331–6336.